remote sensing

MDPI

Article

Artificial-Intelligence-Based Classification to Unveil Geodynamic Processes in the Eastern Alps

Christian Bignami [1,*], Alessandro Pignatelli [1], Giulia Romoli [1] and Carlo Doglioni [1,2]

[1] Istituto Nazionale di Geofisica e Vulcanologia, 00143 Rome, Italy; alessandro.pignatelli@ingv.it (A.P.); giulia.romoli@ingv.it (G.R.); carlo.doglioni@ingv.it (C.D.)
[2] Earth Science Department, Sapienza University of Rome, 00185 Rome, Italy
* Correspondence: christian.bignami@ingv.it

Abstract: InSAR has emerged as a leading technique for studying and monitoring ground movements over large areas and across various geodynamic environments. Recent advancements in SAR sensor technology have enabled the acquisition of dense spatial datasets, providing substantial information at regional and national scales. Despite these improvements, classifying and interpreting such vast datasets remains a significant challenge. InSAR analysts and geologists frequently have to manually analyze the time series from Persistent Scatterer Interferometry (PSI) to model the complexity of geological and tectonic phenomena. This process is time-consuming and impractical for large-scale monitoring. Utilizing Artificial Intelligence (AI) to classify and detect deformation processes presents a promising solution. In this study, vertical ground deformation time series from northeastern Italy were obtained from the European Ground Motion Service and classified by experts into different deformation categories. Convolutional and pre-trained neural networks were then trained and tested using both numerical time-series data and trend images. The application of the best performing trained network to test data showed an accuracy of 83%. Such a result demonstrates that neural networks can successfully identify areas experiencing distinct geodynamic processes, emphasizing the potential of AI to improve PSI data interpretation.

Keywords: multi-temporal InSAR; neural networks; deformation classification

Citation: Bignami, C.; Pignatelli, A.; Romoli, G.; Doglioni, C. Artificial-Intelligence-Based Classification to Unveil Geodynamic Processes in the Eastern Alps. *Remote Sens.* **2024**, *16*, 4364. https://doi.org/10.3390/rs16234364

Academic Editors: Maria Kaselimi and Benedikt Soja

Received: 11 September 2024
Revised: 25 October 2024
Accepted: 20 November 2024
Published: 22 November 2024

1. Introduction

Is Artificial Intelligence (AI) a useful tool for solving big-data analysis in the domain of geophysical studies? In our research, we want to give some answers and hints on using AI to address the classification and identification of deformation processes, starting from Multi-temporal Synthetic Aperture Radar Interferometry (MT-InSAR).

Multi-temporal InSAR is nowadays one of the most-used techniques to study and monitor ground movements in different geodynamic regimes [1]. Thanks to the recent technological advances of SAR sensors, several actors can provide wider area coverage with very dense spatial information, allowing the analysis at regional, national, and continental scales. Despite that, the huge amount of information is not always easy to interpret and classify, especially in the domain of ground motion analysis [2–4]. The identification of different types of geological or geodynamics processes, and consequently the spatial clusterization of the temporal evolution of crustal deformations, still need some efforts. Typically, the results obtained from MT-InSAR are provided in terms of mean ground velocity or acceleration. These simplified representations do not provide a clear understanding of surface displacement changes in time and become very critical when, for example, dealing with strong nonlinear processes, periodic behavior, or any combination of stable/no motion states and sudden acceleration. These representations mask the complexity of geological and tectonic (and many other) phenomena. The InSAR interpreters should check point by point the InSAR time series of Persistent Scatterers Interferometry output,

a process that is extremely time-consuming (maybe impossible at a regional or national scale). In such a context, post-processing MT-InSAR data could benefit from the application of AI algorithms.

AI has been used in several applications based on remote-sensing data, demonstrating its effectiveness in image processing, particularly for case studies focused on object classification, land cover and use, and change detection [5]. Conversely, there are a few works where AI has been used for deformation analysis. An interesting publication from [6] reviews the successful applications of AI on Earth science. Here, a few examples concern geohazards based on machine-learning approaches, such as predicting earthquakes' magnitude and location and discriminating between volcanic tremors, lava fountains, and other events in volcanic monitoring applications. All these works do not deal with InSAR and ground deformation measurements. Some attempts based on remote-sensing data (acquired by optical sensors) have been made for landslide identification.

One of the pioneering works on the use of AI has been proposed by [7]. They exploited a Neural Network (NN) trained using simulated interferograms to estimate seismic source parameters. The work aimed to skip the unwrapping procedure that often introduces errors (i.e., phase jumps) into the estimation of ground deformations caused by an earthquake.

Similarly, ref. [8] used a Convolutional Neural Network (CNN) to classify interferometric fringes in wrapped interferograms obtained from the Sentinel-1 mission, for the identification of sudden unrest over approximately 900 volcanoes.

In ref. [9], some applications of deep learning and SAR are presented. The paper reports applications in different domains of SAR, including object detection, terrain classification, despeckling, and InSAR. The latter is still dealing with single interferograms and noisy fringes for restoring unwrapping errors.

The forecasting of volcanic activities and unrest using deep learning (based on a CNN trained with synthetic data) is shown in some papers, such as [10,11]. The authors demonstrate the ability of such methods to both locate deformation and classify the type of deformation in single interferograms or in time series of wrapped interferograms. For example, volcanic unrest applications are presented by [10], where a self-supervised learning approach is proposed and successfully applied to the dyke intrusions and consequent inflation phenomenon that occurred at Fagradalsfjall volcano, Reykjanes Peninsula, Iceland, on January 2020 and on March 2021. Similarly, a CNN has been exploited to classify InSAR interferograms containing deformation patterns to detect seismic events [12], where the authors designed a supervised CNN, called SarNet, trained with one million noise-free synthetic interferograms generated by the Okada, 1985 forward model [13].

An exercise on InSAR time series is carried out by [14], where Sentinel-1 data, elaborated over the Azufre volcanic complex (Central Andes, at the border of Argentina and Chile), are analyzed. Neural networks are used to reconstruct time series of deformation, aiming to reduce the input features for clustering purposes.

An interesting work, proposed by [15], uses point-wise InSAR time-series data provided by the European Ground Motion Service (EGMS) to identify anomalous movements on buildings in Rome, Italy. The authors adopted an unsupervised learning algorithm to train the network and then exploited the AI-based algorithm to detect buildings affected by trend anomalies (i.e., gradual changes in mean velocity), noise anomalies (i.e., high variability of motion), and step anomalies (i.e., sudden changes).

From this review of published papers, it is clear how the use of AI has not been deeply investigated for InSAR time-series analysis when applied to large-area monitoring. Our work aims to provide some evidence of the potential capabilities of AI algorithms to uncover tectonic and geological (non-linear) processes that are very often hidden in the huge datasets available from multi-temporal InSAR data.

For such a purpose, we exploited four different neural networks that have been trained with labeled data obtained by visual inspection InSAR time series. Despite the high time-consuming step of selecting the training data, and the reduced amount of labeled information concerning the huge quantity of point measurements and related

time series (less than 2% of the whole dataset) covering our study area, the results are encouraging. The final map highlights clusters of points located in different regions, spatially homogeneous and in agreement with the expected regional trends.

2. Materials and Methods

We have applied the AI algorithm to an area in the northeastern part of the Italian territory that corresponds to a portion of the Veneto, Trentino-Alto Adige, and Friuli regions, and includes Alpine and pre-Alpine foothills and plains morphological areas (Figure 1). This sector of Italy represents the retrobelt of the Alpine orogen generated by the subduction of the European Plate beneath the Adriatic Plate. The study area is characterized by southwest verging thrusts of Cretaceous to present thrusts and its foreland basin [16,17] (Figure 2). It features widespread, mostly Mesozoic, passive continental margin carbonatic sequences lying on a Variscan Paleozoic metamorphic basement. The Belluno Syncline also contains Cenozoic active margin sequences (flysch and molasse), deposited in the Venetian foreland basin at the front of the uplifting southern Alps retrobelt front. The same basement and sedimentary cover sequences are buried in the present subsiding Venetian foreland. Present shortening of less than 2 mm/yr has been measured by GPS data in a cross-section of the area, testifying to an SSE motion of the eastern Alps. Moreover, horizontal velocities indicate a stable trend (less than half mm/yr) of the Veneto–Friuli plain. GPS vertical data report an uplift up to about 2 mm/yr in the mountainous area, mainly on the north of the Mt. Grappa–Mt. Cesen anticline, while a maximum of 2 mm/yr subsidence rate has been recorded in the foreland basin using both GNSS and InSAR data, a rate that decreases, moving from the coast towards the eastern Alps, along the already mentioned SSE direction and is hence in agreement with the horizontal shortening [18]. Finally, GPS data in this area are affected by hydrological and karst effects, which may continuously modify the deformation rates [19].

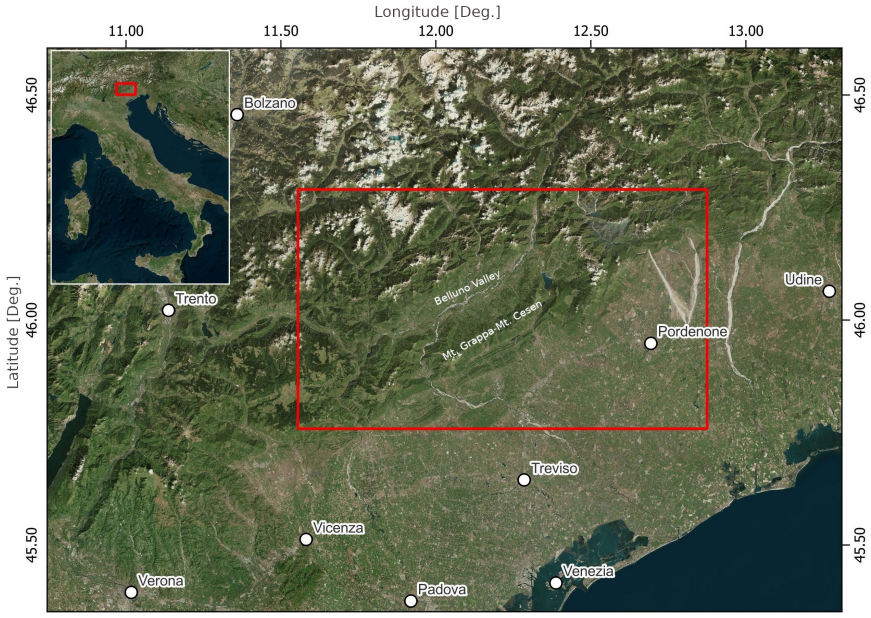

Figure 1. Topographic map of the study area (framed in red) for which ground motion data have been downloaded and analyzed by means of AI algorithms.

We have taken advantage of the European Ground Motion Service (EGMS) [20] to download Mean Ground Velocity (MGV) maps and Time Series (TS) of deformation of our area of interest, the latter being the objective of the classification test. The EGMS provides multi-temporal InSAR products over the whole European continent. The service is free, and any user can collect ground deformation data derived by processing images of the Copernicus Sentinel-1 SAR mission. The EGMS provides maps of deformation from

ascending and descending satellite orbits, and their projections on vertical and east–west directions. For our experiments, we downloaded and analyzed only the vertical projection (Figure 3), which is the most relevant considering the expected slow deformation processes that are on-going in this region. Vertical deformation products are derived by combining measurements collected on ascending and descending orbital passes of the Sentinel-1 mission, and they are available at 100 m per pixel (gridded points).

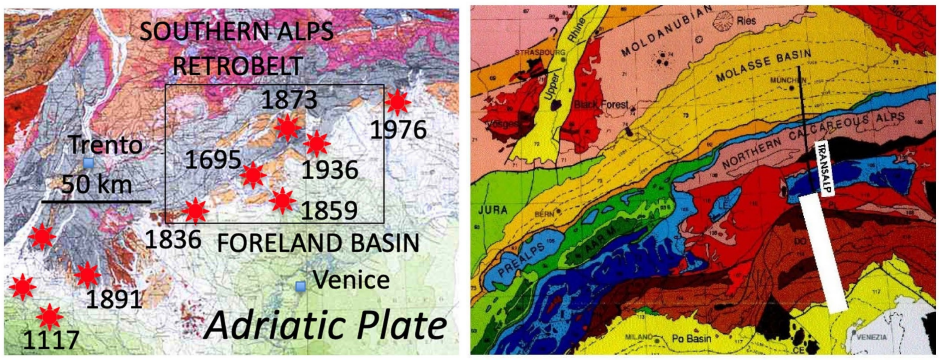

(**a**) (**b**)

Figure 2. (**a**) Structural model of the study area. Red stars show the most energetic earthquakes in the area: 1117, Verona M 6.6; 1695, Asolo M 6.5; 1836, Bassano M 5.5; 1873, Cansiglio M 6.1; 1936, Cansiglio M 6.5; 1976, Friuli M 6.5. The study area is obliquely separated by the growing Alps at the northwestern side and the Venetian foreland basin plain in the southeastern corner. (**b**) Geological map of the area of interest (see black rectangle in (**a**)).

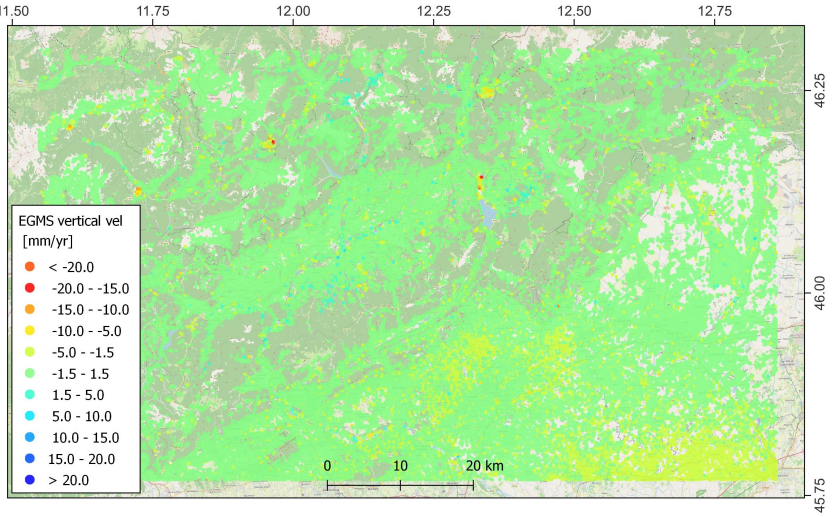

Figure 3. The extracted EGMS products. The map reports the mean ground velocity in vertical directions. Positive values mean uplift and negative values mean subsidence. The figure shows an almost totally stationary region, i.e., with zero mean ground velocities, with a few spots characterized by negative trends (subsidence; see red/orange pixels on the map). Light negative trends are also visible in the southwest part of the map.

The current dataset is related to the MGV spanning from January 2016 to December 2021, and each TS is composed of 364 measurements of deformation, i.e., about 180 images per orbit. Such a product represents our sole source of data to train and test the AI algorithms. This step is crucial because there are currently no labeled InSAR time series available, which significantly impacts the accuracy of the final classification. The training set selection of the deformation trends has been performed manually. A human operator, through a dedicated web application, assigned to each of the selected points the most relevant trend by observing its plot of InSAR deformation time series and choosing among

eight available classes of deformation implemented in the web application. The latter have been identified on the basis of the most common trends that typically can be observed in InSAR multi-temporal products: linear stable, linear subsidence, linear uplift, periodic stable, periodic subsidence, periodic uplift, accelerating, and decelerating. Note that the last two trends refer to deformation time series with the positive and negative concavity of a second-order polynomial trend, or when stable trends present downwards or upwards behaviors (see Figure 4b).

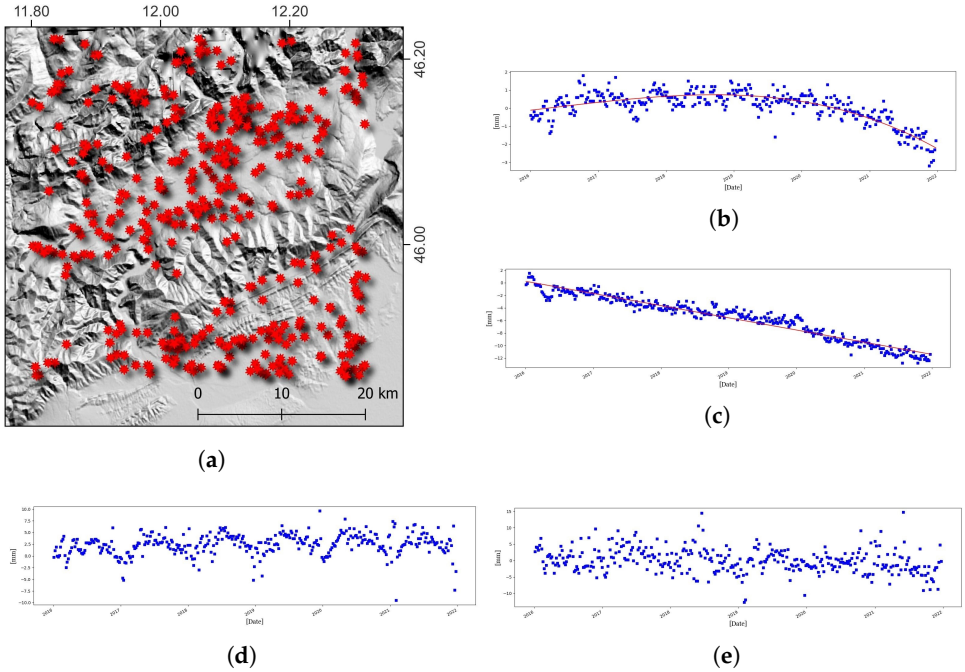

Figure 4. (**a**) Spatial distribution of the labeled time series. Red stars represent the labeled records. The map highlights the good and not spatially clustered selection of the training set, homogeneously spread out in the study area. (**b**) Example of continuous deceleration trend. (**c**) Example of linear down trend. (**d**) Example of periodic trend. (**e**) Example of noisy TS, where no dominant trend of deformation can be observed. These types of TS are expected to be miss-classified, hence reducing the accuracy of the AI classification. This is why this type of time series has not been included in the training procedure.

We have labeled 422 points over 34,053 subsets, which represent about 1.24% of the entire dataset. The labeling operation was extremely difficult and time-consuming (almost 10 working hours).

The resulting class distribution is shown in Table 1. It is worth noting that the selected training set is spatially well distributed over the area of interest, as reported in Figure 4a. This testifies that the deformation trends are not biased in some specific regions and guarantees that all the possible tectonic and geological processes are considered.

Table 1. Percentage of representativeness of each class after the labeling task.

Label	Count	Percent
Decelerating	116	27.49%
Linear Down	104	24.64%
Linear Stable	75	17.77%
Periodic Stable	36	8.53%
Periodic Down	36	8.53%
Linear Up	33	7.82%
Periodic Up	17	4.03%
Accelerating	5	1.18%

Table 1 highlights a clear unbalanced distribution; hence, specific methods need to be addressed during the training task of the NN (see Appendix A).

It is worth mentioning that TS are always affected by noise, because of the accuracy of the MT-InSAR techniques and by unwanted disturbances, such as atmospheric phase screen, that impact the displacements estimates. Typically, a few mm of noise affects each TS record; therefore, especially when the deformation signals are small and subtle, i.e., close to the sensitivity of the technique, the TS appear very noisy (see Figure 4e). It is not easy to figure out how many TS records do not present a clear and strong deformation trend, but taking into account the typical low rates characteristic of our study area (e.g., [18]), we can expect that a not negligible number of records are noisy and deprived of any dominant trend. Finally, it is worth noticing that atmospheric residual signals typically introduce periodic oscillations in the InSAR time series, usually due to semi-annual wet and dry seasons. The selection of these types of classes (see Table 1) has been considered with the objective to identify areas where such residuals are dominant.

Two distinct training processes were undertaken to develop an automatic system for classifying time series. Specifically, we utilized two different types of input data to identify the one yielding the best results.

The first type of dataset comprises numerical time-series data, i.e, all the sample data in the time series are used. In our case, each time series contains the deformation values, in mm, at each SAR image; therefore, we have 364 samples per series. The second type involves images of time-series plots. The use of images as input data is motivated by the availability of several pre-trained neural networks for image processing. A pre-trained network is a neural network that has been previously trained on a large dataset and can be used as a foundation for further training on a new, often smaller, dataset. This approach leverages the features and patterns learned during the initial training, enhancing performance and reducing the training time required for the new task. Some well-known examples of a pre-trained network are AlexNet [21–23], EfficientNet [24], and ImageNet [25].

While the architecture of pre-trained neural networks is basically already optimized, for the convolutional 1D, which was used for numerical time-series input data, some of the architecture details have to be defined, such as, for example, the number of convolutional layers, the number of filters, and the filter size. In order to define such parameters we have applied a Bayesian optimization technique [26] aimed at tuning such values in order to maximize network accuracy. By means of this procedure, we could be confident that we were using the best network architecture and hyperparameters.

To ensure a successful training process and accurate results, it is standard practice to divide the available dataset into three groups: training, test, and validation data. In this context, the actual classifications for all three groups are known. The test data group is not used during the training process but is reserved for final evaluation to compare the network's classifications against the true labels, thus assessing accuracy. This test, alongside the accuracy estimated using the training data, allows for the evaluation of the network's generalization capability. If the classification accuracy for the training data significantly exceeds that of the test data, it indicates an overfitting problem.

When data are limited or the machine-learning method is not computationally intensive, using test data at the end of the training process is sufficient. However, when training is time-consuming, it is advantageous to monitor potential overfitting during the process and stop if necessary. This is achieved using the validation data. At specified intervals, the validation data are used similarly to the test data. If a substantial difference between training and validation accuracy is observed, the training process is halted. Ultimately, the test data are always employed to estimate the overall method accuracy.

To evaluate the quality of the final results, rather than using the simple accuracy value, a well-known confusion matrix is used. A confusion matrix is a table used to evaluate the performance of a classification algorithm by comparing the actual and predicted classifications. Each row of the matrix represents the instances of an actual class, while each

column represents the instances of a predicted class. For a classification task with n classes, the confusion matrix will be an n×n matrix. The element at the i-th row and j-th column of the matrix indicates the number of instances of class i that were predicted as class j. The main diagonal elements (where i = j) represent the number of instances that were correctly classified, while the off-diagonal elements represent misclassifications.

This structure allows for a detailed analysis of the classifier's performance, providing insights into not only the overall accuracy but also the types and frequencies of errors made.

3. Results

The training was conducted using a dataset of 422 classified time series, divided into 296 time series for training, 42 for validation, and 84 for testing. The main topic of this work is not to find the best network to classify the time series but to demonstrate the potentiality of such an approach to automatically identify their patterns. However, to obtain a reliable solution we used the most common approaches to these types of data. More specifically, as described in the Materials and Method section, the training process involved two approaches:

1. Applying a 1D Convolutional Neural Network (CNN) to the numerical time-series data. A 1D convolutional layer is a neural network layer designed to process sequential data by sliding a filter along one dimension to capture local patterns. It is commonly used in tasks involving time series, being computationally efficient [27]. The hyperparameters of such a network have been tuned by means of a Bayesian optimization.
2. Using AlexNet, EfficientNet, and ImageNet as pre-trained networks to analyze numerical series plot images. AlexNet is a pioneering CNN architecture that revolutionized computer vision by winning the 2012 ImageNet competition. It consists of multiple convolutional and fully connected layers, designed to efficiently process large-scale image data. Key innovations include the use of ReLU activation, dropout for regularization, and GPU acceleration [23]. EfficientNet is a family of CNN architectures designed to achieve higher accuracy with fewer parameters. It uses a compound scaling method that uniformly scales the depth, width, and resolution of the network to improve efficiency. EfficientNet models provide a better balance between performance and computational cost, making them popular for image classification and other vision tasks [28]. ImageNet is a large-scale image dataset designed for visual object recognition research. It contains millions of labeled images across thousands of categories and has been the benchmark for major advancements in deep learning, particularly in image classification. The ImageNet Large Scale Visual Recognition Challenge (ILSVRC) has played a pivotal role in driving innovations in CNNs, allowing them to achieve high accuracy in image classification tasks [29].

More specifically, for case (1) we have optimized the following hyperparameters:

1. The number of convolution layers (from 1 to 5);
2. The number of filters of each convolution layer (from 1 to 10);
3. The size of the filters (from 1 to 10);
4. The learning rate (from 1×10^{-8} to 1×10^{2}).

The hyperparameters showing the best accuracy are shown in Table 2:

Table 2. Hyperparameter settings after Bayesian optimization.

N. Filters	Filter Size	Convolution Layers Number	Learning Rate
6	7	1	32.367

The results are presented in the following confusion matrices, and accuracy is summarized in Table 3. Specifically, Figure 5a displays the confusion matrix for the 1D CNN, while Figure 5b shows the confusion matrix for the pre-trained AlexNet and Figure 5c,d for

EfficientNet and ImageNet, respectively. Notably, AlexNet demonstrates a significantly higher accuracy.

Table 3. Summary of confusion matrices for the four trained NNs.

	1D CNN	AlexNet	EfficientNet	ImageNet
Overall accuracy	0.726	0.833	0.571	0.798
K-coefficient	0.653	0.792	0.433	0.747

Table 3 also reports K-coefficient (Cohen's kappa) values for the proposed networks. Cohen's kappa coefficient has been defined by [30] and is a statistical measure that provides a robust evaluation of the accordance of two independent classification models by performing a statistical difference test between the observed concordance with the one expected by chance. For all networks, K-coefficients are positive, suggesting that the classification outcomes are not merely random.

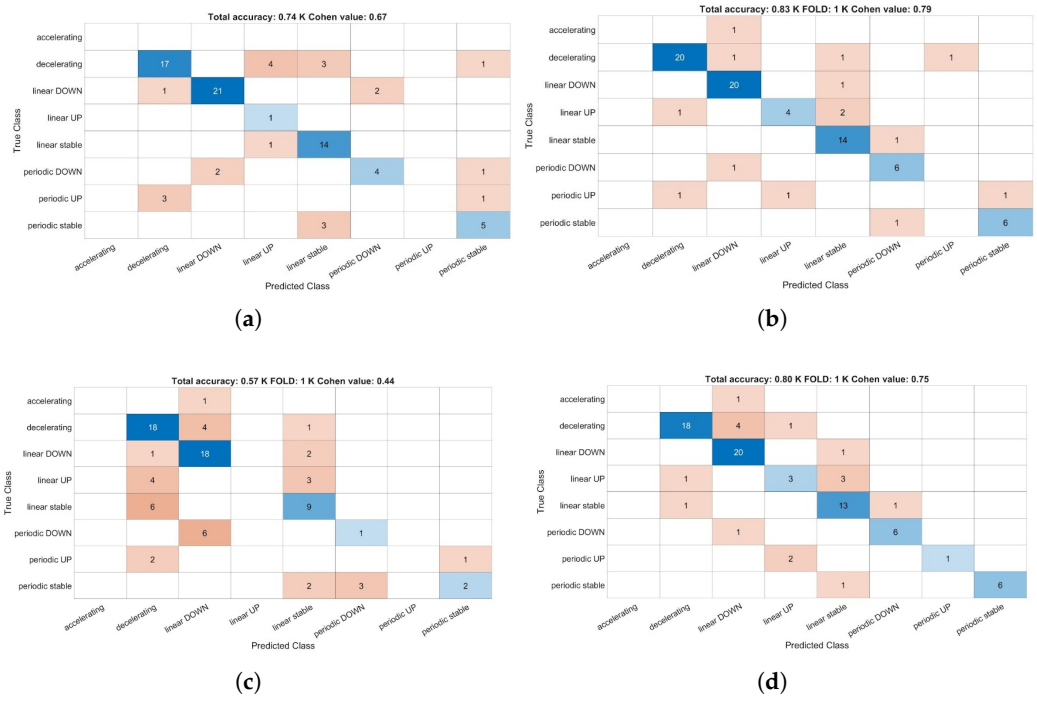

Figure 5. (**a**) Confusion matrix after applying the 1D CNN trained network to test data. (**b**) The same, but for the AlexNet trained network. (**c**) For the EfficientnNet trained network. (**d**) For the ImageNet trained network. Accuracy and K-coefficient (Cohen's kappa) values for the proposed networks are summarized in Table 3.

Using the AlexNet-trained neural network, we predicted the classifications for all the TS in the study area (more than 110,000 records), with the results shown in Figure 6. The number of classified elements are listed in Table 4. Since the time series are associated with specific coordinates, we mapped these classifications onto a geo-referenced map (classification map). The map allows the identification of at least four different clusters of points, enabling an initial regional classification of the geodynamic processes at first glance.

Table 4. Number of classified elements for each class. The two columns refer to the name given to the specific trend and the number of time series assigned to that class, according to the procedure detailed in the Materials and Methods section.

Class	N. Elements
Linear Down	46,182
Linear Stable	35,456
Decelerating	11,941
Periodic Stable	10,029
Periodic Down	6463
Linear Up	1787
Periodic Up	1145
Accelerating	5

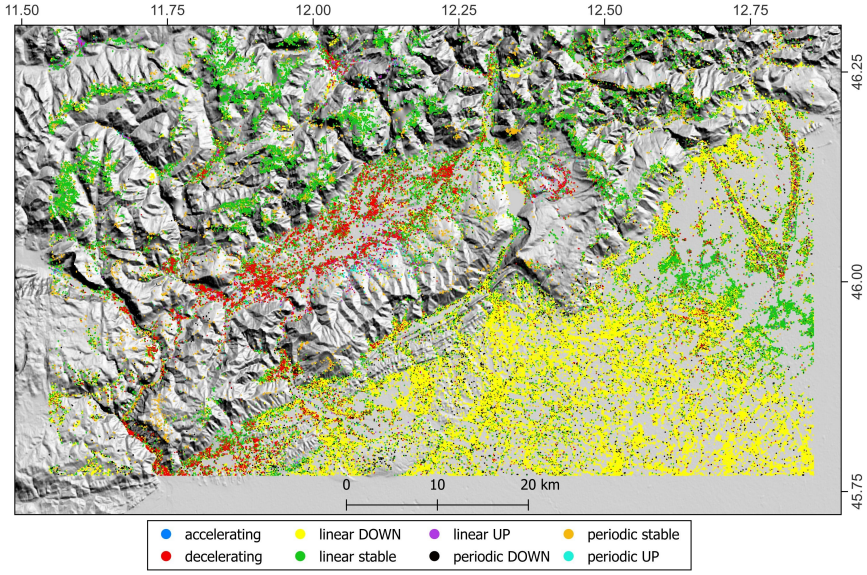

Figure 6. Trend classification map obtained from InSAR time series and AI algorithm. The maps clearly allow one to identify some clusters of points belonging to the same class of deformation. The purple-magenta points show the uplifting sector of the Alpine area, whereas the yellow dots illustrate the subsiding foreland basin. A relatively stable area (green points) is dominant in the northwest sector of the analyzed areas. The red cluster refers to the decorating trends in the Belluno valley.

In Figure 6, two dominant clusters identify the linear subsidence and the linear stable trend, namely yellow points and green points, respectively. The cluster of red points is mainly positioned in the Belluno Valley, where decelerating trends, i.e., negative concavity of the displacement time series, represent the leading ground motion. The fourth visible cluster is the purple-magenta one. The latter is concentrated in the Mt.Grappa and Mt. Cesen chain. Note that the acceleration trend is not shown taking into account the only five points belonging to such a class of deformation.

4. Discussion

In order to better figure out the spatial distribution of the classified time series, and hence identify the geodynamic processes occurring in the area, we report the maps of each class in Figure 7. The figure shows the main four clusters already discussed and presented in Figure 6 and highlights how the periodic signals seem to be associated with the corresponding linear trends (i.e., linear down/periodic down, linear up/periodic up, and so on). It is also worth noting that all the types of deformation trends are scattered over the whole area because of the following:

1. the intrinsic noise of the InSAR time series;
2. the inevitable miss-classifications due to the 80% overall accuracy of the CNN.

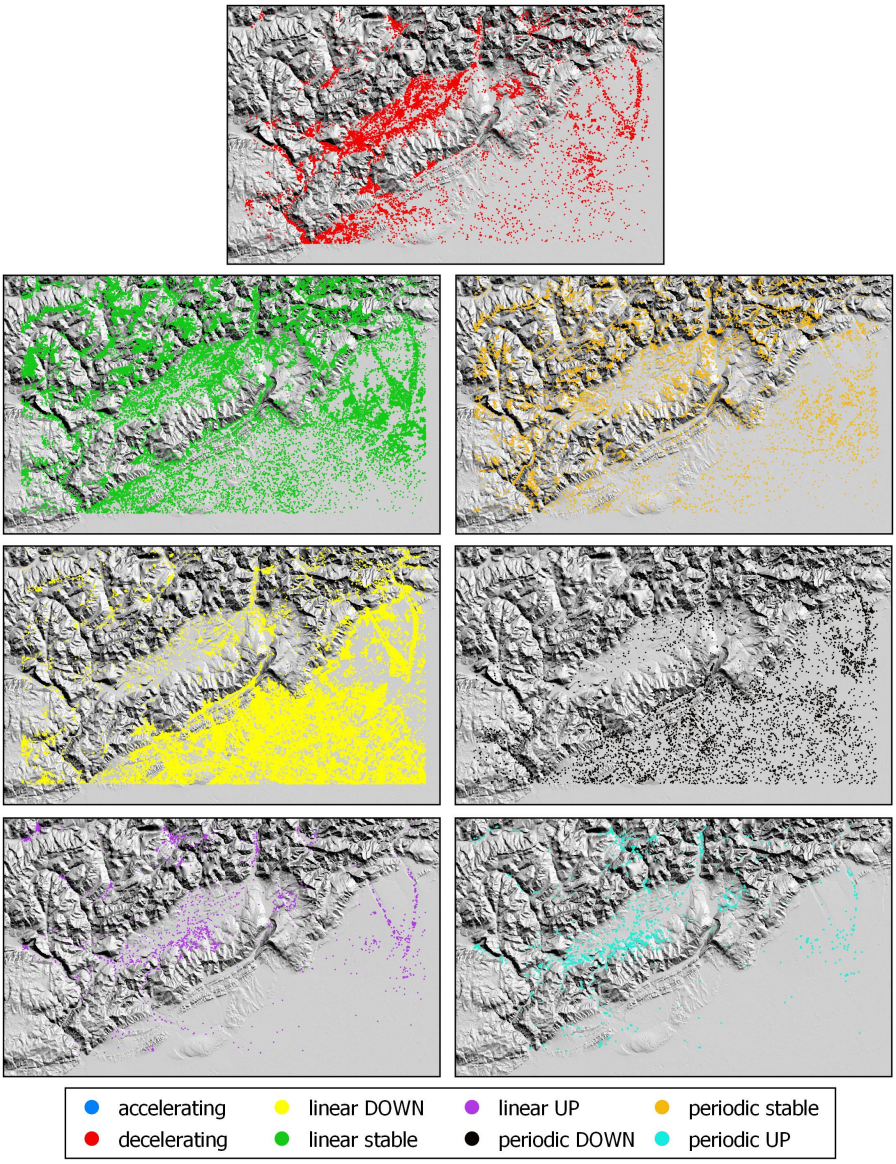

Figure 7. Maps of each classified deformation trend.

The spatial analysis of the classified TS has also been carried out by performing a spatial density map, also known as a heatmap, for the seven TS clusters, and the result is shown in Figure 8. The seven maps allow a better understanding of where each specific TS has been localized in our area of interest, confirming the following:

1. The deceleration trend is highly concentrated within the Belluno basin, hence the ground motions show an uplift or stable behavior in the first part of the TS and then tend to go down (see example in Figure 4);
2. The stable trend is mainly concentrated in the Alpine and pre-Alpine retrobelt, with a small pattern located in the northeastern section of the Po plain;
3. The downward motion is markedly dominant in the foreland basin;
4. The uplifting behavior seems to be a very local phenomenon concentrated over the Mt. Grappa–Mt. Cesen anticline;
5. The periodic signals are strongly correlated with homologous linear trends (compare left and right columns in Figure 8). The period of the oscillations is of approximately one year, with minima of the displacement around December–January of each year,

and the maxima approximately in May–June. This is likely due to the atmospheric phase screen, which is linked to the water vapor content that typically affects radar signal delay [31]. Such periodicity is superimposed on all the TS and is much more evident when the amount and rate of deformation is very small.

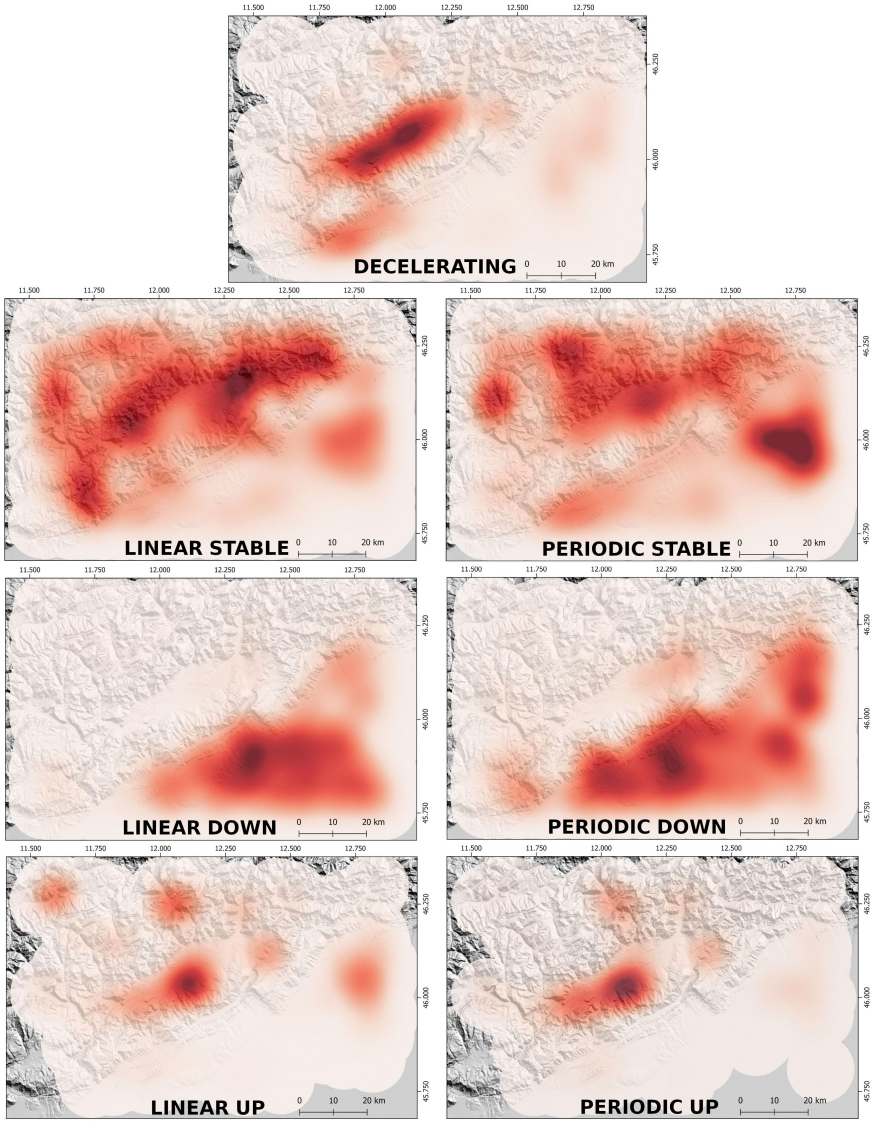

Figure 8. Heatmaps (density of points) for each classified deformation cluster of points. The higher the density, the darker the red.

The four main identified spatial clusters match the expected deformation processes controlled by the tectonic setting. The subduction of the European Plate beneath the Adriatic Plate is causing the ongoing contraction of the Alpine orogen. The study area of this research is the southern Alps, representing the retrobelt of the Alps, with active SE-verging thrusts, uplifting the Earth's surface and moving toward their subsiding foreland basin represented by the Venetian Plain [17,18]. This geodynamic setting is compatible with the observed slow subsidence affecting the Venetian plain and the ongoing uplift of the anticline of Mt. Grappa and Mt. Cesen. For example, linear down and linear up ground motions are in very good (spatial) agreement with the observed trends by GPS data (compare Figure 2 in [18] with the corresponding classification maps in Figure 7 and heatmaps in Figure 8).

The almost stable cluster and the vertical deceleration cluster within the Belluno valley (green and red points in Figures 6 and 9) can be justified by the relative horizontal velocity that appears to temporally decrease in the Alpine retrobelt.

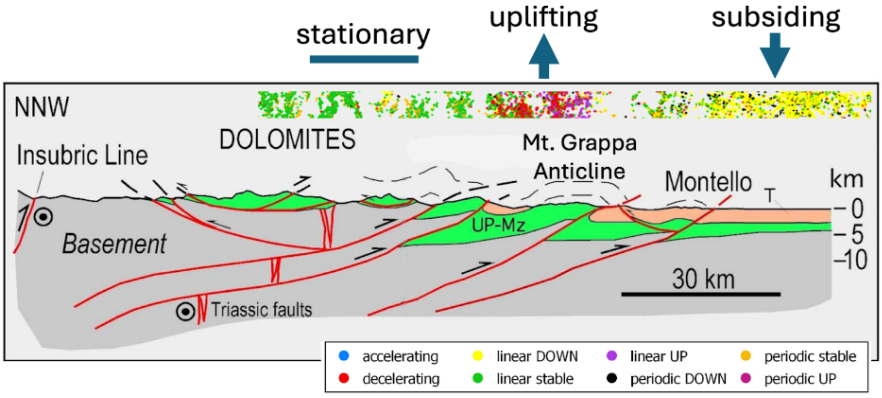

Figure 9. Cross section of the study area and of the superimposed TS classification by means of the proposed AI method (modified after [16]). The figure highlights the agreement between the different ground motion types and the tectonic setting.

Concerning the comparison between image-based neural network classification (AlexNet) and time-series neural networks (1D CNN), the results indicate that AlexNet outperforms the 1D CNN in this case. It is important to state that all input signals were used in their raw form, without any pre-processing or additional elaboration. This choice has been purposely done for two reasons:

1. We were more interested in having a method working as fast as possible without any human intervention;
2. A comparison of the two datasets including pre-processing would require a more extensive analysis, as it depends on the various parameters of the chosen pre-processing methods. There may not be a one-size-fits-all solution, as different pre-processing techniques might perform better with different network architectures. Addressing this is part of our future research plans.

5. Conclusions

In the eastern southern Alps affected by a shortening of about 2 mm/yr, the analysis confirms the ongoing uplift of the Mt. Grappa anticline and the subsidence in the Venetian foreland basin, where the Montello anticline represents the forefront of the Alpine retrobelt. It is noteworthy that the plateau of the inner part of the belt in the Dolomites is relatively stable. The results of this study show that, despite certain limitations, the neural network used for time-series classification provides a highly effective and practical solution to a task that would otherwise be nearly impossible for human analysis.

The inherent complexity and volume of the time-series data involved—encompassing a vast array of patterns and subtle variations—make manual classification not only impractical but also virtually impossible within a reasonable timeframe. Despite the model's imperfections, such as occasional misclassifications or sensitivity to noise, its ability to process and categorize thousands of time series efficiently underscores its value. The trade-off between accuracy and feasibility highlights the necessity of automated methods like neural networks in handling large-scale time-series data, where human intervention would be prohibitively time-consuming and error-prone.

In summary, the present work permits us to draw some important findings:

1. AI, when properly trained, is able to unveil different geological processes, often hidden in the InSAR mean ground velocity maps.
2. The implemented algorithm can automatically classify huge dataset of InSAR point time series, discriminating against a variety of deformation trends.

3. The clustered deformation trends highlight spatially and localized deformation phenomena, in agreement with the tectonic and geodynamic settings.
4. The trade-off between accuracy and feasibility highlights the necessity of automated methods like AI in handling large-scale time-series data, where human intervention would be prohibitively time-consuming and error-prone.

It is important to note that the use of neural networks does not enhance the reliability of time-series classification compared to human analysis; rather, it enables the same level of classification quality to be achieved at a significantly faster pace.

Author Contributions: The authors contributed to all aspects of the paper's content and its drafting. Furthermore, the manuscript emerged from ongoing interaction, proposal, and discussion among them. To elaborate: C.B. conceived the idea, selected the dataset, and performed the manual classification; A.P. and G.R. decided the artificial intelligence approaches and implemented the code to realize the task; C.D. detailed the geological aspects of the paper. All authors have read and agreed to the published version of the manuscript.

Funding: This work has been partially funded by the "PIANETA DINAMICO–SAFARI" and the "Reti Multiparametriche" projects of the Italian National Institute of Geophysics and Volcanology (INGV).

Data Availability Statement: Link to European Ground Motion Service (EGMS) products: https://egms.land.copernicus.eu/(accessed on January 2024). Vertical deformation products are derived by combining measurements collected on ascending and descending orbital passes of the Sentinel-1 mission and can be downloaded from the same link.

Conflicts of Interest: The authors declare no conflicts of interest.

Abbreviations

The following abbreviations are used in this manuscript:

AI	Artificial Intelligence
CNN	Convolutional Neural Network
EGMS	European Ground Motion Service
GNSS	Global Navigation Satellite System
MGV	Mean Ground Velocity
MT-InSAR	Multi-temporal SAR Interferometry
NN	Neural Network
SAR	Synthetic Aperture Radar
SE	South-East
TS	Time Series

Appendix A

AI nowadays represents a revolution in almost all the applications dealing with huge datasets coming from different domains. Its usage spans science, computer vision, economy and finance, security, and many others. As a result, these approaches have garnered significant attention across various domains, including healthcare diagnostics, financial decision-making, facial recognition, fraud detection, and many others. The primary benefits associated with the application of machine-learning methodologies are as follows:

1. Adaptability and Universality: Machine-learning models demonstrate exceptional adaptability, necessitating only minor adjustments, predominantly related to input data, to tackle a wide range of problems. This flexibility negates the requirement for meticulous efforts in pinpointing domain-specific mathematical or statistical techniques, as machine-learning algorithms inherently recognize and adjust to such patterns or methodologies;
2. Efficacy through Data Acquisition: The primary focus lies in supplying sufficient data to support the machine's learning mechanism for problem resolution. Subsequently, the system independently and automatically addresses similar problems across di-

verse contexts, assuming these contexts exhibit similarities with the supplied data. The machine-learning ability to extrapolate from the provided data can be assessed following the learning phase;

3. Resilient Performance with Diverse Data: Machine-learning methods frequently deliver impressive outcomes, even in situations where the accessible data display diversity;
4. Objective Analysis: Although machines cannot supplant human judgment, the absence of emotional bias in algorithms proves beneficial by reducing statistical biases. Objective analysis helps circumvent subjective influences that humans may inadvertently introduce.

Machine-learning algorithms can be categorized into two primary types: supervised and unsupervised methods [32].

Supervised learning algorithms learn from a dataset where the correct answers are known, and they make predictions or decisions based on input data to approximate the correct outputs. Common examples of supervised learning tasks include regression (predicting continuous values) and classification (predicting categorical labels). For example, supervised methods in stock market analysis aim to predict variables such as stock prices, trading volume, and market trends when provided with other variables like historical prices, trading volume, and economic indicators. In forecasting the closing price of a particular stock for the next trading day, various predictors such as today's closing price, trading volume, and relevant economic news can be utilized. In these contexts, training a machine-learning model for stock price prediction, it is crucial to supply it with historical stock market data, including both the predictors (e.g., closing price, trading volume, economic indicators) and the corresponding outcomes (e.g., next day's closing price). This dataset, consisting of predictors and corresponding outcomes, is known as labeled data. During the training phase, the machine-learning algorithm identifies patterns and correlations between the predictors and outcomes from the provided data. Once the model is successfully trained, it can autonomously predict the closing price of the stock for the next trading day based on the available predictors. The primary advantage of machine learning in this context is that human involvement is predominantly required before the training phase. After adequate training, the system can independently produce accurate forecasts, reducing the necessity for continuous human intervention in the prediction process.

Unsupervised machine-learning techniques, particularly clustering, represent a fundamental method for grouping similar data points within a dataset. The identification of similarity among records depends on various mathematical metrics inherent to the specific algorithm utilized. For instance, in the healthcare sector, clustering algorithms are employed to categorize patient profiles based on medical histories, demographic details, and diagnostic information.

Artificial Neural Networks (ANNs) fall under the category of supervised machine-learning methodologies, as outlined by [32]. Drawing inspiration from the architecture of the primate cerebral cortex, ANNs are structured to progressively distill abstract features from input data to optimize the desired output, as discussed by [33,34].

Fundamentally, ANNs consist of multiple layers of interconnected neurons. The input data are fed into the initial layer, where each datum undergoes processing by an individual neuron. These neurons implement specific transfer functions, contingent upon the specific ANN architecture employed. Upon processing the input data in one layer, the resultant outputs are forwarded to the subsequent layer. In this layer, each neuron's input is a linear combination of the outputs from the preceding layer, defined by a set of coefficients known as neuron weights. This sequential processing continues through all layers until it reaches the final layer, referred to as the "output layer". In this layer, the generated outputs are juxtaposed with the provided labels. After comparing the true labels with the predicted values, a backward propagation mechanism is initiated to refine the neuron weights. This propagation process involves iteratively adjusting a parameter vector to minimize the discrepancies between the actual and predicted values, as articulated by [35].

Convolutional Neural Networks (CNNs) represent a specialized category of artificial neural networks acclaimed for their adeptness in extracting localized features from matrices. Their architecture is notably intricate, predominantly composed of layers of filters applied to matrices, as delineated by [35]. This unique configuration enables each neuron within a CNN to focus on a restricted subset of inputs or neurons from the preceding layer, rather than processing information from the entire set. A comprehensive exposition on CNNs would necessitate considerable elaboration and exceeds the aim of this study. For an exhaustive comprehension of CNNs, we advocate consulting works by [33,34]. Within this section, we present an overview of the salient components of CNNs, encompassing four distinct layer types: convolutional layers, pooling layers, fully connected layers, and a singular softmax layer, as articulated by [33].

Convolutional layers emerge as a pivotal constituent for dissecting local features, enabling each neuron to scrutinize specific segments of the input data. This methodology guarantees that each neuron evaluates unique data sub-regions. After the convolutional layers, pooling layers are frequently integrated to diminish data dimensions. For instance, a 2×2 convolutional output matrix undergoes replacement by its maximal value.

Fully connected layers assume a critical function within the CNN framework by transmuting the output matrix. Ordinarily, the initial fully connected layer in a CNN is succeeded by additional fully connected layers that reconfigure the output from a 2D matrix to a 1D vector, as expounded by [36]. For illustration, a fully connected layer might represent a 6×4 matrix as a singular vector comprising 24 elements.

Consequently, the output from the fully connected layers is channeled to the softmax layer, which translates the weights from the terminal fully connected layer into probabilities corresponding to each potential label. Ultimately, the predicted label is aligned with the label possessing the maximal probability value.

When creating and refining a neural network, it is crucial to carefully select and optimize a set of hyperparameters. Although [37] provide a thorough explanation of the differences between parameters and hyperparameters and a detailed description of hyperparameters, we will offer a brief overview here.

In the context of a neural network, "parameters" usually refer to the weights of the connections between neurons, which are the numerical values that the model learns during training. Conversely, "hyperparameters" are determined before training begins and relate to the network's structure, the methods used for optimization, the division of data into training and testing sets, and various other considerations.

Some examples of hyperparameters with a brief explanations are the following:

1. Network architecture: This involves the number and the type of layers in the sequence. In the case of convolutional layers, this includes how many filters and their size;
2. Learning rate: This hyperparameter determines the size of the steps taken during the optimization process to adjust the model's weights;
3. Dropout Percentage: This hyperparameter involves randomly deactivating some neurons in each iteration. This hyperparameter determines the proportion of neurons that are turned off during training. This is generally used to avoid overfitting.

References

1. Moreira, A.; Prats-Iraola, P.; Younis, M.; Krieger, G.; Hajnsek, I.; Papathanassiou, K.P. A tutorial on synthetic aperture radar. *IEEE Geosci. Remote Sens. Mag.* **2013**, *1*, 6–43. [CrossRef]
2. Fabris, M.; Battaglia, M.; Chen, X.; Menin, A.; Monego, M.; Floris, M. An integrated InSAR and GNSS approach to monitor land subsidence in the Po River Delta (Italy). *Remote. Sens.* **2022**, *14*, 5578. [CrossRef]
3. Lazos, I.; Papanikolaou, I.; Sboras, S.; Foumelis, M.; Pikridas, C. Geodetic Upper Crust Deformation Based on Primary GNSS and INSAR Data in the Strymon Basin, Northern Greece—Correlation with Active Faults. *Appl. Sci.* **2022**, *12*, 9391. [CrossRef]
4. Shen, G.; Fu, W.; Guo, H.; Liao, J. Water Body Mapping Using Long Time Series Sentinel-1 SAR Data in Poyang Lake. *Water* **2022**, *14*, 1902. [CrossRef]
5. Farooq, B.; Manocha, A. Satellite-based change detection in multi-objective scenarios: A comprehensive review. *Remote Sens. Appl. Soc. Environ.* **2024**, *34*, 101168. [CrossRef]

6. Sun, Z.; Sandoval, L.; Crystal-Ornelas, R.; Mousavi, S.M.; Wang, J.; Lin, C.; Cristea, N.; Tong, D.; Carande, W.H.; Ma, X.; et al. A review of Earth artificial intelligence. *Comput. Geosci.* **2022**, *159*, 105034. [CrossRef]
7. Stramondo, S.; Del Frate, F.; Picchiani, M.; Schiavon, G. Seismic source quantitative parameters retrieval from InSAR data and neural networks. *IEEE Trans. Geosci. Remote Sens.* **2010**, *49*, 96–104. [CrossRef]
8. Anantrasirichai, N.; Biggs, J.; Albino, F.; Hill, P.; Bull, D. Application of machine learning to classification of volcanic deformation in routinely generated InSAR data. *J. Geophys. Res. Solid Earth* **2018**, *123*, 6592–6606. [CrossRef]
9. Zhu, X.X.; Montazeri, S.; Ali, M.; Hua, Y.; Wang, Y.; Mou, L.; Shi, Y.; Xu, F.; Bamler, R. Deep learning meets SAR: Concepts, models, pitfalls, and perspectives. *IEEE Geosci. Remote Sens. Mag.* **2021**, *9*, 143–172. [CrossRef]
10. Bountos, N.I.; Papoutsis, I.; Michail, D.; Anantrasirichai, N. Self-supervised contrastive learning for volcanic unrest detection. *IEEE Geosci. Remote Sens. Lett.* **2022**, *19*, 3003905. [CrossRef]
11. Beker, T.; Ansari, H.; Montazeri, S.; Song, Q.; Zhu, X.X. Deep learning for subtle volcanic deformation detection with InSAR data in central volcanic zone. *IEEE Trans. Geosci. Remote Sens.* **2023**, *61*, 5218520. [CrossRef]
12. Brengman, C.M.J.; Barnhart, W.D. Identification of surface deformation in InSAR using machine learning. *Geochem. Geophys. Geosy.* **2021**, *22*, e2020GC009204. [CrossRef]
13. Okada, Y. Surface deformation due to shear and tensile faults in a half-space. *Bull. Seismol. Soc. Am.* **1985**, *75*, 1135–1154. [CrossRef]
14. Ansari, H.; Rubwurm, M.; Ali, M.; Montazeri, S.; Parizzi, A.; Zhu, X.X. InSAR displacement time series mining: A machine learning approach. In Proceedings of the 2021 IEEE International Geoscience and Remote Sensing Symposium IGARSS, Brussels, Belgium, 11–16 July 2021; pp. 3301–3304.
15. Kuzu, R.S.; Bagaglini, L.; Wang, Y.; Dumitru, C.O.; Braham, N.A.A.; Pasquali, G.; Santarelli, F.; Trillo, F.; Saha, S.; Zhu, X.X. Automatic Detection of Building Displacements Through Unsupervised Learning From InSAR Data. *IEEE J. Sel. Top. Appl. Earth Obs. Remote Sens.* **2023**, *16*, 6931–6947. [CrossRef]
16. Doglioni, C.; Carminati, E.A.M. *Structural Styles and Dolomites Field Trip*, 1st ed.; Memorie descritt. Carta Geol. d'Italia; Poligrafico dello Stato: Rome, Italy, 2008.
17. Doglioni, C. The Venetian Alps thrust belt. In *Thrust Tectonics*; McClay, K.R., Ed.; Springer: Dordrecht, The Netherlands, 1992; pp. 319–324. ISBN 978-0-412-43900-1.
18. Anderlini, L.; Serpelloni, E.; Tolomei, C.; De Martini, P.M.; Pezzo, G.; Gualandi, A.; Spada, G. New insights into active tectonics and seismogenic potential of the Italian Southern Alps from vertical geodetic velocities. *Solid Earth Discuss.* **2020**, *11*, 1681–1698. [CrossRef]
19. Serpelloni, E.; Pintori, F.; Gualandi, A.; Scoccimarro, E.; Cavaliere, A.; Anderlini, L.; Belardinelli, M.E.; Todesco, M. Hydrologically induced karst deformation: Insights from GPS measurements in the Adria-Eurasia plate boundary zone. *J. Geophys. Res. Solid Earth* **2018**, *123*, 4413–4430. [CrossRef]
20. Costantini, M.; Minati, F.; Trillo, F.; Ferretti, A.; Novali, F.; Passera, E.; Dehls, J.; Larsen, Y.; Marinkovic, P.; Eineder, M.; et al. European ground motion service (EGMS). In Proceedings of the 2021 IEEE International Geoscience and Remote Sensing Symposium IGARSS, Brussels, Belgium, 11–16 July 2021; pp. 3293–3296.
21. Han, X.; Zhong, Y.; Cao, L.; Zhang, L. Pre-trained alexnet architecture with pyramid pooling and supervision for high spatial resolution remote sensing image scene classification. *Remote Sens.* **2017**, *9*, 848. [CrossRef]
22. Indolia, S.; Goswami, A.K.; Mishra, S.P.; Asopa, P. Conceptual understanding of convolutional neural network-a deep learning approach. *Procedia Comput. Sci.* **2018**, *132*, 679–688. [CrossRef]
23. Krizhevsky, A.; Sutskever, I.; Hinton, G.E. ImageNet classification with deep convolutional neural networks. *Commun. ACM* **2017**, *60*, 84–90. [CrossRef]
24. Taner, A.; Öztekin, Y.B.; Duran, H. Performance analysis of deep learning CNN models for variety classification in hazelnut. *Sustainability* **2021**, *13*, 6527. [CrossRef]
25. Russakovsky, O.; Deng, J.; Su, H.; Krause, J.; Satheesh, S.; Ma, S.; Huang, Z.; Karpathy, A.; Khosla, A.; Bernstein, M.; et al. ImageNet large scale visual recognition challenge. *Int. J. Comput. Vis.* **2015**, *115*, 211–252. [CrossRef]
26. Gelbart, M.A.; Snoek, J.; Adams, R.P. Bayesian optimization with unknown constraints. *arXiv* **2014**, arXiv:1403.5607.
27. Goodfellow, I. *Deep Learning*; MIT Press: Cambridge, MA, USA, 2016.
28. Tan, M.; Le, Q. Efficientnet: Rethinking model scaling for convolutional neural networks. *Int. Conf. Mach. Learn. Pmlr* **2019**, *97*, 6105–6114.
29. Deng, J.; Dong, W.; Socher, R.; Li, L.-J.; Li, K.; Li, F.-F. ImageNet: A large-scale hierarchical image database. In Proceedings of the 2009 IEEE Conference on Computer Vision and Pattern Recognition, Miami, FL, USA, 20–25 June 2009.
30. Cohen, J. A coefficient of agreement for nominal scales. *Educ. Psychol. Meas.* **1960**, *20*, 37–46. [CrossRef]
31. Hanssen, R.F. *Radar Interferometry: Data Interpretation and Error Analysis*; Remote Sensing and Digital Image Processing; Springer: Dordrecht, The Netherlands, 2001; ISBN 978-0-7923-6945-5.
32. Lantz, B. *Machine Learning with R*; Community experience distilled; Packt Publishing: Birmingham, UK, 2013; ISBN 978-1-78216-215-5.
33. O'Shea, K.; Nash, R. An introduction to convolutional neural networks. *arXiv* **2015**, arXiv:1511.08458.
34. Rawat, W.; Wang, Z. Deep convolutional neural networks for image classification: A comprehensive review. *Neural Comput.* **2017**, *29*, 2352–2449. [CrossRef]

35. Cao, Q.; Parry, M.E. Neural network earnings per share forecasting models: A comparison of backward propagation and the genetic algorithm. *Decis. Support Syst.* **2009**, *47*, 32–41. [CrossRef]
36. Pignatelli, A.; D'Ajello Caracciolo, F.; Console, R. Automatic inspection and analysis of digital waveform images by means of convolutional neural networks. *J. Seismol.* **2021**, *25*, 1347–1359. [CrossRef]
37. Zhu, W.; Beroza, G.C. PhaseNet: A deep-neural-network-based seismic arrival-time picking method. *Geophys. J. Int.* **2019**, *216*, 261–273. [CrossRef]